JOURNAL OF GEOPHYSICAL RESEARCH, VOL. 105, NO. D22, PAGES 27,037–27,047, NOVEMBER 27, 2000

A generalized algorithm for retrieving cloudy sky skin temperature from satellite thermal infrared radiances

Menglin Jin

Department of Meteorology, University of Maryland, College Park

Robert E. Dickinson

Earth and Atmospheric Sciences, Georgia Institute of Technology, Atlanta

Abstract. A physical algorithm for calculating cloudy pixel skin temperature from its neighboring clear pixels is proposed generalizing that of *Jin* [2000]. Two neighboring pixels over the same land cover have a difference in temperature largely explained by surface insolation. Hence this algorithm starts from the surface energy balance equation (SEB) and expresses each energy term of SEB as a function of skin temperature. Then SEB is solved to derive cloudy pixel skin temperature from neighboring clear skin temperature plus a correction term determined by surface insolation, air temperature, and wind speed. This algorithm can be used for nights and winter hemisphere high latitudes where there is no surface insolation and is applicable to any surface where the principle of SEB is applicable. The algorithm is evaluated by using FIFE and BOREAS field experiments. Its global application has been examined through simulations with the NCAR Community Climate Model (CCM) coupled with the Biosphere-Atmosphere Transfer Scheme (BATS) simulations. The accuracy of the algorithm is encouraging: the rms error at a monthly pixel level is 1–2 K. Observed errors are greater when there is precipitation.

1. Introduction

Satellite thermal infrared radiances retrieve so-called skin temperatures [*Susskind*, 1992; *Dickinson*, 1992; *Jin et al*., 1997]. These temperatures are useful for computation of surface-air flux, detection of convection, and evaluation of models. Such temperatures cannot be obtained from measurement of upward longwave radiation as obtained from AVHRR or EOS MODIS when the surface is masked by clouds. However, many applications of skin temperature require this information at all times [*Jin and Dickinson*, 1999]. Plate 1 shows global radiative temperature over a day in July 1992, from the NOAA/NASA pathfinder AVHRR land data set. The difficulty of obtaining skin temperature everywhere from such data is illustrated by the regions that are cooler by more than 15 K than their surrounding areas and must be tops of clouds. Any thermal infrared imagery is similarly limited in its ability to provide surface temperature data sets.

Jin [2000] (hereinafter referred to as Jin99) initially addressed this question through use of a hybrid technique. The method correlated sensible, latent, and longwave fluxes with net solar radiation, to derive the skin temperature for a pixel obscured by clouds from a neighboring clear pixel. It was tested against field experiments and GCM simulations. This paper modifies the Jin99 method by relating surface fluxes to T_s and hence uses surface energy balance to solve for T_s. Such an approach is physically based and readily generalizes to any underlying surface that satisfies a constraint of energy balance.

Consistent with Jin99, the proposed method considers clouds to affect surface temperature by changing the surface insolation and downward longwave radiation, which in turn are redistributed into sensible, latent, or soil heat fluxes. Therefore the skin temperature of a cloudy pixel (T_s^{cld}) can be obtained from its neighboring clear pixel skin temperature (T_s^{clr}) and the difference of surface energy balance between the two pixels, for example, net solar radiation (ΔS_n), net longwave radiation (ΔR_n), sensible heat flux (ΔH), latent heat flux (ΔE), and ground heat flux (ΔG).

Surface skin temperature variations are driven by variations in surface insolation as affected by sky conditions, and hence the law of energy conservation as it governs surface-temperature–related physical processes is used here as the theoretical basis of our proposed algorithm. The values of T_s^{cld} are inferred from neighboring T_s^{clr} and surface energy balance (SEB). The alternative of determining it entirely from measured cloud properties does not appear practical because of complexity and lack of usable relationships between clouds and surface temperature. In addition, SEB itself already includes the influences of sky conditions on the surface. Surface insolation decreases when cloudiness increases [*Li et al*., 1993], and downward longwave radiation depends on cloud base temperature [*Fu and Liou*, 1992].

This generalized method requires both satellite measurements (T_s^{clr}, surface insolation) and surface data (air temperature T_a, wind speed U). The latter are usually operationally available from routine weather station observations. One potential problem is that these observations provide information regarding the atmospheric surface layer but may be unrepresentative of neighboring areas. *Shuttleworth* [1991] pointed out that data from a single site can be used to represent a large-scale area if it is taken over a comparatively uniform, well-watered surface with a fairly weak precipitation gradient and that it is consistently and reliably available over a long period.

The next section describes the methodology. Section 3 evaluates the methodology with FIFE and BOREAS observations.

Paper number 2000JD900318.
0148-0227/00/2000JD900318$09.00

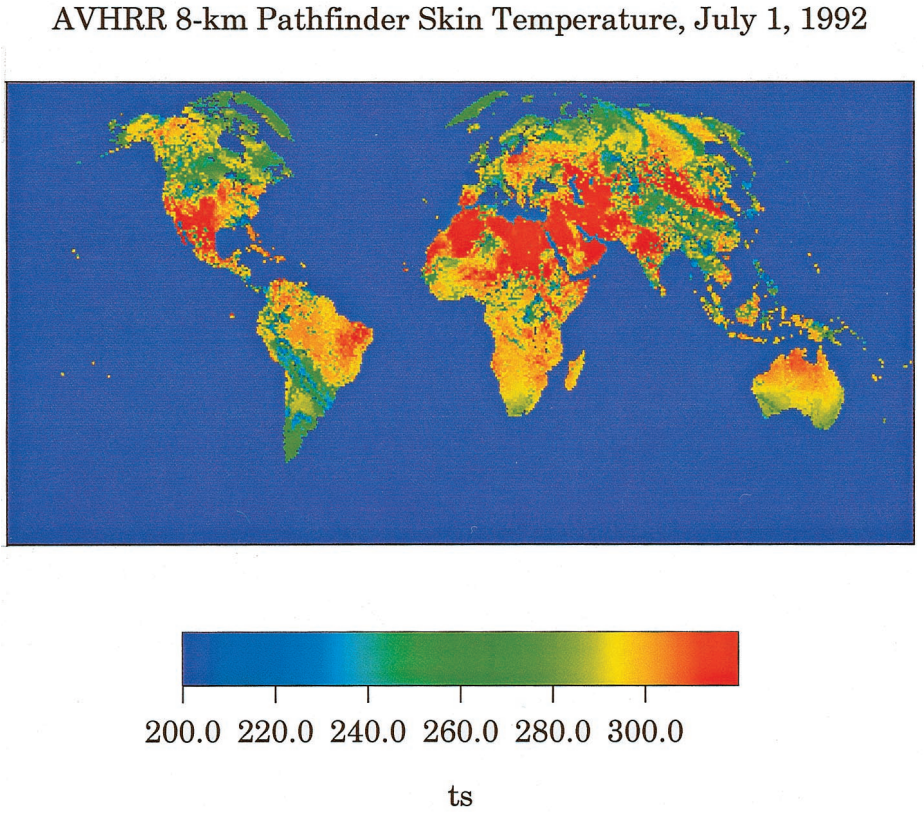

Plate 1. Skin temperature of one day in July 1992 from AVHRR. The spatial resolution is 8 km. Data are provided by NOAA/NASA Pathfinder land surface data sets.

In addition, we test the algorithm on CCM3-/BATS-produced global data sets to examine its global application. Results presented here suggest that overall, this method is very encouraging for normal surfaces with rms of about 1–2 K over a month and at pixel resolution. A large rms error occurs at times of heavy precipitation. The final part of this paper discusses the strengths and limitations of this method and how it might be applied to global areas using satellite measurements.

2. Methodology

Energy balance at the surface is assumed to be determined by

$$H + E + G = S_n - R_n, \tag{1}$$

where H is sensible heat flux, E is latent heat flux, G is energy stored by canopy and soil, S_n is net solar absorbed by canopy and soil, and R_n is net longwave radiation. All terms are in W m^{-2}. The annual mean of G is near zero at most locations. Equation (1) omits energy exchanges from changes between solid and liquid phases (snow melting, soil freezing, etc.)

2.1. Determination of Neighboring Clear Pixel

Following Jin99, the "neighboring clear pixel" algorithm (hereinafter referred to as "the NP algorithm" in this text) is used. For one cloudy pixel, if there is a clear pixel close to it either spatially or temporally and it is over the same surface vegetative/soil type, the two pixels are considered as "neighboring" here. The surface type of each pixel could be known from a land cover map where the whole globe is divided into several vegetation types. The cloudiness condition for each pixel could be determinated from the temperature threshold technique that was used in the International Satellite Cloud Climatology Project (ISCCP) [*Rossow*, 1983]. As pointed out in Jin99, spatial distances of less than 100–300 km and temporal distances of about 2 days are considered as "close" in this work.

One cloudy pixel may have multiple neighboring clear pixels. We need to assign weighting that would be given for multiple clear pixels. Jin99 argued, based on spatial and temporal autocorrelations, that clear pixels for the previous two days or within 300 km could be equally weighted.

A cloudy pixel differs in temperature from a neighboring clear pixel largely because of the different surface insolation. With "Δ" representing the difference between the clear and the cloudy pixels the NP approach is written as

$$\Delta H + \Delta E + \Delta G = \Delta S_n - \Delta R_n. \tag{2}$$

To apply this approach, each energy term in (2) is further expressed in terms of skin temperature. By solving (2), we could derive T_s^{cld} from its neighboring T_s^{clr} and a correction term related to surface insolation, air temperature, and wind speed.

2.2. Sensible Heat Flux

Sensible heat flux is given by

$$H = a(T_s - T_a), \tag{3}$$

where T_a is air temperature, T_s is skin temperature, and a is $\rho C_p C_{DH} U$. C_p is specific heat, C_{DH} is the drag coefficient for heat flux, and U is wind speed; a is generally in the range of 10 W m^{-2} K^{-1} (short vegetation) to 100 W m^{-2} K^{-1} (tall vegetation). For two neighboring pixels,

$$\Delta H = H_1 - H_2, \tag{4}$$

$$H_1 = \rho c_p C_{DH} U_1 (T_{s1} - T_{a1}), \tag{5}$$

$$H_2 = \rho c_p C_{DH} U_2 (T_{s2} - T_{a2}), \tag{6}$$

where the subscripts "1" and "2" stand for cloudy pixel and its neighboring clear pixel, respectively.

2.3. Latent Heat Flux

Latent heat flux is connected to sensible heat flux through the Bowen ratio B (see equation (5.2.7) in the work of *Gratt* [1992]):

$$B = \frac{H}{E}. \tag{7}$$

The Bowen ratio usually varies with season, location, and weather. Furthermore, since the transpiration component of latent heat flux depends on vegetation properties, such as the stomates, plant age, and water stress of the plant, the resistance to water flux also varies. This interdependences of evapotranspiration, soil wetness, surface vegetation conditions, and surface insolation makes determining the Bowen ratio problematical.

A commonly used approximation for the Bowen ratio is that suggested by *Priestly and Taylor* [1972]. The Priestly-Taylor method first introduced a concept of "equilibrium" Bowen ratio, B_e, to the evaporation into a saturated atmosphere from a wet surface (e.g., as also discussed by *Dickinson* [1988]). Because the relative humidity is generally less than 100%, evaporation from short vegetation but moist soil generally exceeds this "equilibrium evaporation" by some factor α, which Priestly-Taylor argued was on average $\alpha = 1.26$.

Let

$$\Gamma_e = \frac{1}{1 + B_e} \tag{8}$$

be the relative amount of net energy that goes into equilibrium evaporation. The Priestly-Taylor Bowen ratio, B_{PT}, is related to the ratio of evaporation to the equilibrium evaporation and given by [e.g., *Garratt*, 1992, equation (5.2.9)]

$$B_{PT} = \frac{1 - \Gamma_e \alpha}{\Gamma_e \alpha}. \tag{9}$$

Obviously, B_{PT} is a function of both α and T, i.e., $B_{PT}(\alpha, T)$. If two neighboring pixels have the same surface, they are likely to have nearly the same α.

The α compensates for neglecting of evaporation contributed by the aerodynamic component [*Garratt*, 1992], allowing the equations to be useful for unsaturated conditions [*Stull*, 1988]. The term α has been found to have a wide range of values. Under conditions of minimal advection for low roughness length sites, experimental data show $\alpha \approx 1.26 \pm 0.05$ [*Brustaert*, 1982]. For a well-watered surface, $\alpha = 1.25$ [*Stull*, 1988]. *Blanken et al*. [1997] found that during the growing period the daytime mean α of the forest is 0.91 ± 0.18, but a full-leaf hazelnut has α as much as 1.22 ± 0.16. Their results imply that α is influenced by canopy conductance, leaf area index (LAI), and canopy architecture. The α can also vary somewhat diurnally and seasonally, as observed from the FIFE and HAPEX experiments [*Shuttleworth*, 1992].

Accuracy of the estimation of latent heat flux depends on the accuracy of α. If the correct value of α is denoted as α_0 and error term as $\delta\alpha$, then

$$\alpha = \alpha_0 + \delta\alpha. \tag{10}$$

The error in latent heat induced from on inaccurate α is obtained by combining (7), (9), and (10),

$$\delta = \left(\frac{H_1 \Gamma_1 \alpha_0}{1 - \Gamma_1 \alpha_0} - \frac{H_2 \Gamma_2 \alpha_0}{1 - \Gamma_2 \alpha_0} \right) \left(\frac{\delta\alpha'}{\alpha_0} \right)^2. \tag{11}$$

Because $\delta\alpha/\alpha_0$ is generally about 0.1–0.2, from observations [*Garratt*, 1992; *Shuttleworth*, 1992], the error in latent heat flux estimation induced by $\delta\alpha$ might be less than 10%.

2.4. Net Longwave Radiation

Net longwave radiation is composed of upward longwave radiation ($\Delta R_\uparrow$) from the surface and downward radiation ($\Delta R_\downarrow$) from the atmosphere. In (2),

$$\Delta R_n = \Delta R_\uparrow - \Delta R_\downarrow. \tag{12}$$

The first term on the right-hand side is a function of surface skin temperature and emissivity which is assumed to be unity,

$$\Delta R_\uparrow = \frac{\partial R_\uparrow}{\partial T_s} \Delta T_s. \tag{13}$$

Since the surface emission is governed by the Stephan-Boltzmann law, approximately,

$$\Delta R_\uparrow = 4 \varepsilon \sigma T_s^3 \Delta T_s, \tag{14}$$

and the second term on the right-hand side said of (12) is

$$\Delta R_\downarrow = R_{\downarrow_1} - R_{\downarrow_2}, \tag{15}$$

where $\Delta R_\downarrow$ is directly controlled by cloud properties such as amount and temperature of cloud base.

Downward longwave radiation ($R_\downarrow$) can be determined in several ways. The most explicit way is from radiative transfer theory, integrating $R_\downarrow$ from the top of the atmosphere to the surface with atmospheric profiles known [*Frouin et al*., 1988; *Fu*, 1992]. Downward longwave radiation from the atmosphere is a function of atmospheric temperature and emittance. The emittance depends on the atmospheric gases (CO_2, H_2O, and O_3) and cloud properties. An explicit calculation of downward longwave radiation using radiative transfer equations is limited by knowledge as to the atmospheric profiles.

Alternatively, empirical formulae have been widely used to estimate downward flux [*Brunt*, 1932; *Swinbank*, 1963; *Idso and Jackson*, 1969; *Brutsaert*, 1975; *Hatfield et al*., 1983; *Culf and Gash*, 1993] but may not be appropriate for global applications because of lack of validation, need for cloud information, and inability to provide the 10 W m^{-2} accuracy required by most applications [*Fung et al*., 1984]. This paper, for simplicity, approximates downward flux similarly to Jin99:

$$\Delta R_\downarrow = b \Delta S_\downarrow + c, \tag{16}$$

where $S_\downarrow$ is the surface insolation and b is a coefficient varying with atmospheric conditions, in particular, cloud amount, cloud level, and water vapor profile. Jin99 finds that this coefficient may have a small range of variation, in general, from 0.1 to 0.17. The parameter c is zero during daylight hours and changes with cloud-base temperature at night.

2.5. Ground Heat Flux

The amplitude of the daily cycle of surface temperature can be significantly greater than that of deeper soil temperature, with timing mainly linked to that of radiation input; thus soil heat flux G, over nonvegetated areas, can be as large as, typically, up to 30% of the net radiation at the surface [*Shuttleworth*, 1992]. With dense vegetation, such as forest, little radiation reaches the ground, and heat storage in the soil can be neglected [*Thom*, 1972]. As suggested by Jin99, soil heat storage is treated by a single slab,

$$G = k_g \frac{\partial T}{\partial Z} = k_g \frac{(T_s - T_d)}{\Delta Z}, \tag{17}$$

where T_d is the sublayer temperature; k_g is the thermal molecular conductivity (W m^{-1} K^{-1}), which is a measure of the ability to conduct heat; and ΔZ is the depth of the sublayer. For an appropriate soil depth, $T_{d1} \approx T_{d2}$; and the T_d terms will be canceled in differencing G between two pixels; that is,

$$\Delta G = \frac{k_g}{\Delta Z} \Delta T_s, \tag{18}$$

where k_g depends on the soil type, and the moisture ΔZ, as defined to be the minimum depth at which two soil pixels have nearly the same temperatures, is ~0.1 m for all soil surfaces.

2.6. Solar Radiation

The ΔS_n component in (2) can be determined from TOA satellite-reflected solar radiation [*Pinker and Ewing*, 1985; *Li et al*., 1993; *Masuda et al*., 1995]. Our proposed method relies on the availability of surface solar radiation, the accuracy of which is, currently, about 10 W m^{-2} [*Li et al*., 1993].

3. Data

3.1. Field Experiment Data

Field experiments of the First International Satellite Land Surface Climatology Project (ISLSCP) Field Experiment (FIFE) and the Boreal Ecosystem-Atmosphere Study (BOREAS) have been employed for algorithm development and evaluation. FIFE was conducted over a 15 km by 15 km area located in central Oklahoma [*Sellers et al*., 1992]. Site-averaged data of skin temperature, air temperature, wind speed, surface fluxes, and precipitation in July 1987 were processed and sampled for half-hour intervals [*Betts*, 1995].

Unlike FIFE which was over a short-grass surface, the BOREAS field experiment was over a high-latitude forest in Canada [*Sellers et al*., 1995]. Surface and atmosphere conditions were observed by portable weather stations, and surface fluxes were obtained through tower measurements. The original measurements were obtained at 15-min intervals and resampled using half-hour intervals.

3.2. Model Simulations

In the absence of generally acceptable and simultaneously measured data sets for the global skin temperature, air temperature, wind speed, and surface insolation, simulations from the NCAR Community Climate Model (CCM3) version 3, coupled with Biosphere-Atmosphere Transfer Scheme (BATS) are used to evaluate the algorithm for global application [*Jin and Dickinson*, 1999]. After model equilibrium has been reached, the monthly mean sea surface temperature in 1995 and the corresponding atmospheric forcing input were used to run the model for an entire year. Hourly model outputs were archived to provide hourly and daily skin temperature, air temperature, and surface radiation and fluxes simulations used in this paper.

4. Results

Two aspects of the NP algorithm are evaluated. First, we examine how reliable it will be for global application, and second, whether coefficients validated for a local area can be used globally with acceptable accuracy tradeoff. As shown in (2) and (3), surface air temperature, wind speed, and ΔS_n are needed in the algorithm. ΔS_n can be derived from satellite remote sensing. Accurate surface air temperature and wind speed most likely could be obtained from surface weather station observations, which if not available may degrade the accuracy of the algorithm.

4.1. Small-Scale Evaluations

The NP approach uses surface energy balance to estimate a cloudy pixel skin temperature as that of its neighboring clear pixel skin temperature plus a correction factor (usually negative) depending on the surface fluxes, air temperature, and wind speed as responsible for the difference between pixels:

$$T_s^{\mathrm{cld}} = T_s^{\mathrm{clr}} + f(\Delta S_n, T_a^{\mathrm{cld}}, T_a^{\mathrm{clr}}, U, \ldots). \tag{19}$$

The second term on the right-hand side could be considered as a correction term related to other factors responsible for the temperature difference between two pixels.

Figure 1 examines our algorithm using two continuous days from FIFE 1987: one clear (Julian day 198) and one cloudy (Julian day 197). Figure 1a presents the clear day skin temperature diurnal cycle ($T_s^{\mathrm{clr}}(t)$, $t = 1, 48$); Figure 1b is the correction term at each half hour; and Figure 1c compares the algorithm-produced skin temperature diurnal cycle ($T_s^{\mathrm{cld}}(t)$, $t = 1, 48$), which is the sum of $T_s^{\mathrm{clr}}(t)$ minus the correction term, with the observations. Skin temperature is calculated by using the algorithm with ΔS_n known from the observations; the other terms were calculated using the methods suggested in section 2. Obviously, the algorithm-produced skin temperatures show good agreement with the ground truth, implying the usefulness of the algorithm. The rms for the whole day (48 values at half-hour intervals) is 0.81 K.

Figure 2 shows the variables that determine the variations of surface temperature, i.e., (a) net solar radiation, (b) downward longwave radiation, (c) upward longwave radiation, (d) sensible heat flux, (e) latent heat flux, and (f) wind speed, all over the FIFE area for the two days used in Figure 1. Evidently, the ΔS_n is as much as 500 W m^{-2} around 0200 LT. Downward longwave radiation for a cloudy day might be expected to be greater because of emission at the cloud-bottom temperature. However, in the presence of precipitation the cloud $R_{\downarrow}$ was lower than that for clear days, possibly from evaporation of rain drops and cloud-base temperatures. In general, the $\Delta R_{\downarrow}$ is about 50 W m^{-2} in the absence of precipitation. In Figure 2c, larger differences in $R_{\uparrow}$ are observed during the day than during the night, consistent with the surface skin temperature differences. Interestingly enough, the shape of $R_{\uparrow}$ is very similar to that of net solar radiation. Sensible heat flux and net solar radiation also have similar diurnal variations, indicating the dependence of sensible flux on solar forcing. At night the sensible heat flux varies little, so there are no obvious differences between cloudy and clear nights. During daylight hours,

sensible heat fluxes on clear days are larger than on cloudy days because of the larger surface-air temperature gradient. The nighttime latent heat flux also varies little (Figure 2e); but daytime latent heat fluxes are substantially larger on clear days than on cloudy ones. The magnitude of E is larger than H for the clear day, and their sum, as much as 550 W m^{-2}, largely balances the surface S_n.

This algorithm requires air temperatures T_a^{clr} and T_a^{cld}, as indicated in (3), to calculate sensible and latent heat fluxes. Obtaining appropriate values may be a difficulty for this NP algorithm. Air temperature, in general, is measured by surface weather stations located irregularly over land surface. In addition to this irregular sampling, the high surface heterogeneity can make the measurement unrepresentative of larger areas. In other words, air temperature data are likely to be unavailable at satellite pixel resolution and globally. To avoid this problem, it may be necessary to relate air to skin temperatures and then use such a relationship to replace T_a in the sensible heat flux (as (3)) so that SEB has one unknown variable, T_s. Figure 3 is a relationship between skin and air temperatures inferred from FIFE observations in July 1987. This relationship depends on many factors, from boundary layer stability to surface vegetative cover to soil moisture, and hence is difficult to describe. Here a linear regression equation is used as a first-order approximation; soon after sunrise, skin temperature is higher than air temperature because the surface insolation increases and exceeds the surface longwave emission [*Jin et al.*, 1997]. Because most of the radiation is absorbed at the surface, the surface temperature increases more rapidly than air temperature. Figure 3b compares skin temperature versus air temperature at night. Because the surface layer is stable at night, both skin and air temperatures vary moderately, and a regression equation can describe this relationship adequately.

The regression relationships concluded from Figure 3 is only a rough approximation. Therefore we need to consider whether less accurate T_a information in the NP algorithm might be sufficient. This is examined in Figure 4, which is designed to evaluate how the absence of accurate air temperature degrades the accuracy of the algorithm.

Figure 4 is the same as Figure 1c except that the air temperatures used here are not the measured ground truth but are calculated from T_s using the linear relationships shown in Figure 3. The overall daytime rms error consequently increases from 0.81 to 2.70 K. However, the large disagreements are found only at and after the occurrence of precipitation; at other times the algorithm-produced and observed skin temperatures are in good agreement. Therefore precipitation occurrence appears to be the primary source of degradation of the estimation of air temperature. One plausible explanation is that at this time the Bowen ratio changes significantly and is quite different from that used by the algorithm, which depends on a predefined α (for example, at the time when the precipitation occurred, the observed Bowen ratio varied significantly from 0.126 to 0.0008, but the calculated Bowen ratio was 0.132,

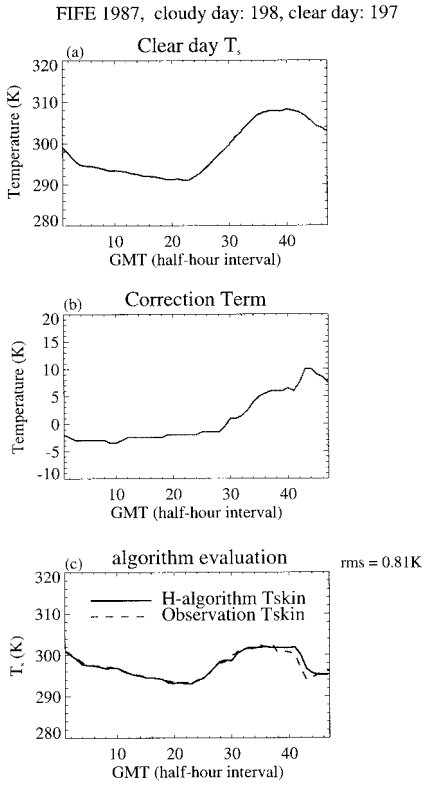

Figure 1. Evaluation of "neighboring-pixel" approach. Data are from FIFE observations for Julian 197 and 198 two days with a half-hour interval. The cloudy skin temperature, $T_s^{\mathrm{cld}}(t)$ (t = 1, 48), can be considered as $T_s^{\mathrm{clr}}(t)$ plus a correction term as described in the text. (a) Skin temperature for clear day, (b) correction term for each interval, and (c) comparison between algorithm-produced cloudy day skin temperature and ground truth. The root-mean-square error (rms) is given at the right-hand top corner.

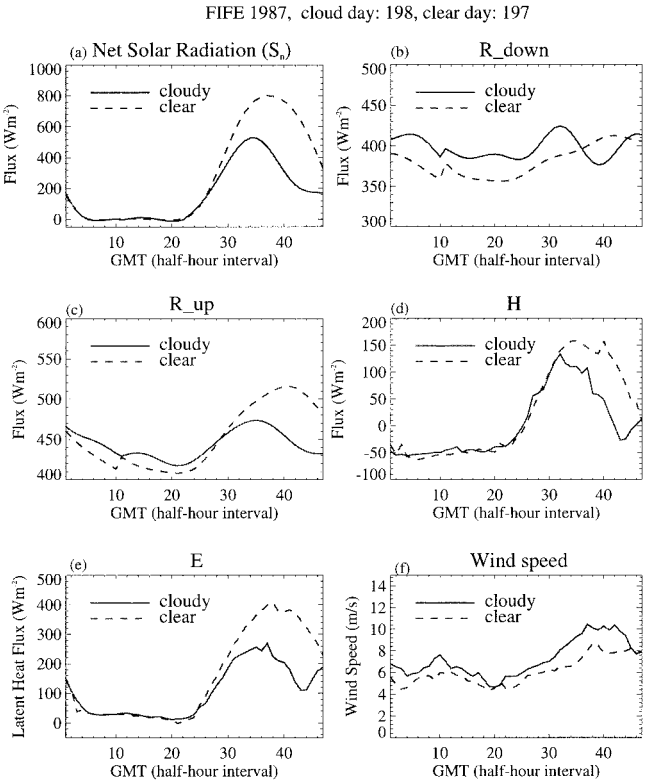

Figure 2. Diurnal cycles of variables used for Figure 1, where Julian day 198 is the cloudy day and 197 the clear day. (a) Net solar radiation, (b) downward longwave radiation, (c) upward longwave radiation, (d) sensible heat flux, and (e) latent heat flux, and (f) wind speed.

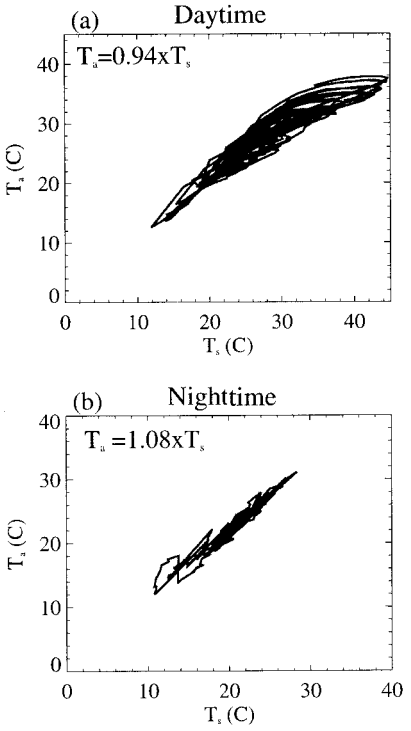

Figure 3. Relationships between skin temperature and air temperature, both in degrees Celsius, based on the FIFE experiment in July 1987. Data for the whole month at half-hour intervals are used for (a) daytime and (b) nighttime. The linear regression equation is given at the right-hand top corner in each panel.

similar to previous hours). Therefore the surface energy terms in SEB may not generate the correct T_s at or soon after precipitation events.

Figure 5 is a further evaluation of the algorithm for the BOREAS forest area. Here spatially adjacent neighboring observations are used. Two BOREAS observing stations are analyzed: one at Prince Albert National Park and the other at Flin Flon. The measurements were sampled when Prince Albert was cloudy and Flin Flon was clear. The rms value shows that on the monthly pixel level, the accuracy of the "neighboring-pixel" algorithm is about 1.77 K. This error is probably an overestimate, because of the use of airport (Flin Flon) which is grass surface, while the other site is forest (Prince Albert National Park).

4.2. Global Evaluations

To examine the global application of the algorithm, we utilize NCAR CCM3/BATS simulations for calculating the T_s from that of the previous day. Use of a GCM simulation instead of real satellite data allows to test the algorithm with physically consistent variables. Plate 2 is the modeled daily global skin temperatures for two continuous days in August: "hb0001" and "hb0002." Daily variations of skin temperatures are noticeable during these two days, in particular, over eastern and central North America, central Asia, southern Africa, Australia, and South America. The prescribed sea surface temperatures, however, vary little from one day to the next (not shown). The land variations are caused by both synoptic and local convection systems.

To evaluate the "neighboring-pixel" approach, we use skin temperature of "hb0002," difference of net solar radiation, air temperature, and surface wind speed between "hb0002" and "hb0001" to derive the skin temperature of "hb0001" day; then we compare the algorithm-based "hb0001" skin temperature with that of modeled "hb0001." In this section we considered original GCM modeled skin temperature as the "truth." Plate 3 is the algorithm-produced land skin temperature using Plate 2b and the difference in solar radiation between these two days, with modeled wind speed and air temperature known. Comparing Plates 3 and 2b shows that the algorithm gives very reasonable skin temperatures agreeing well with the "true" skin temperature in terms of spatial patterns over both sea and land surfaces. This implies that the algorithm can be applied globally with most of the spatial features reproduced.

Plate 4 is the global difference of Plate 2a and Plate 3 (e.g., land only). Again, most areas have an error as small as 1–2 K. However, some extreme values are observed over eastern America and central Asia, where large differences exist in at the original modeled "hb0001" and "hb0002" simulations. The lesser accuracy of the Bowen ratios used in our algorithm is a possible reason for these larger disagreements. In this test we used predefined climatological Bowen ratio for all grids over the same latitude bands. However, when central-eastern Asia had precipitation, its Bowen ratio obviously differed from that of a normal day. This inconsistency could contribute to the disagreement of the final calculated T_s.

Figure 6a is zonal-mean difference of the "true" skin tem-

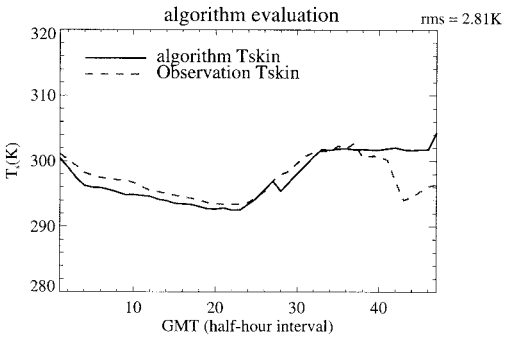

Figure 4. Same as Figure 1f except the air temperature information used in the algorithm is not based on measurement but based on the skin and air temperature relationship derived in Figure 2.

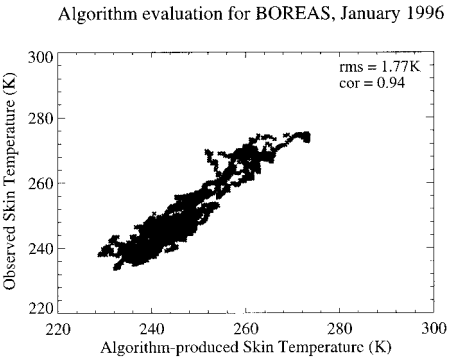

Figure 5. Algorithm evaluation using observations from the BOREAS field experiment in January 1996. The x direction is the algorithm-produced skin temperature and the y direction is the field experiment measured skin temperature.

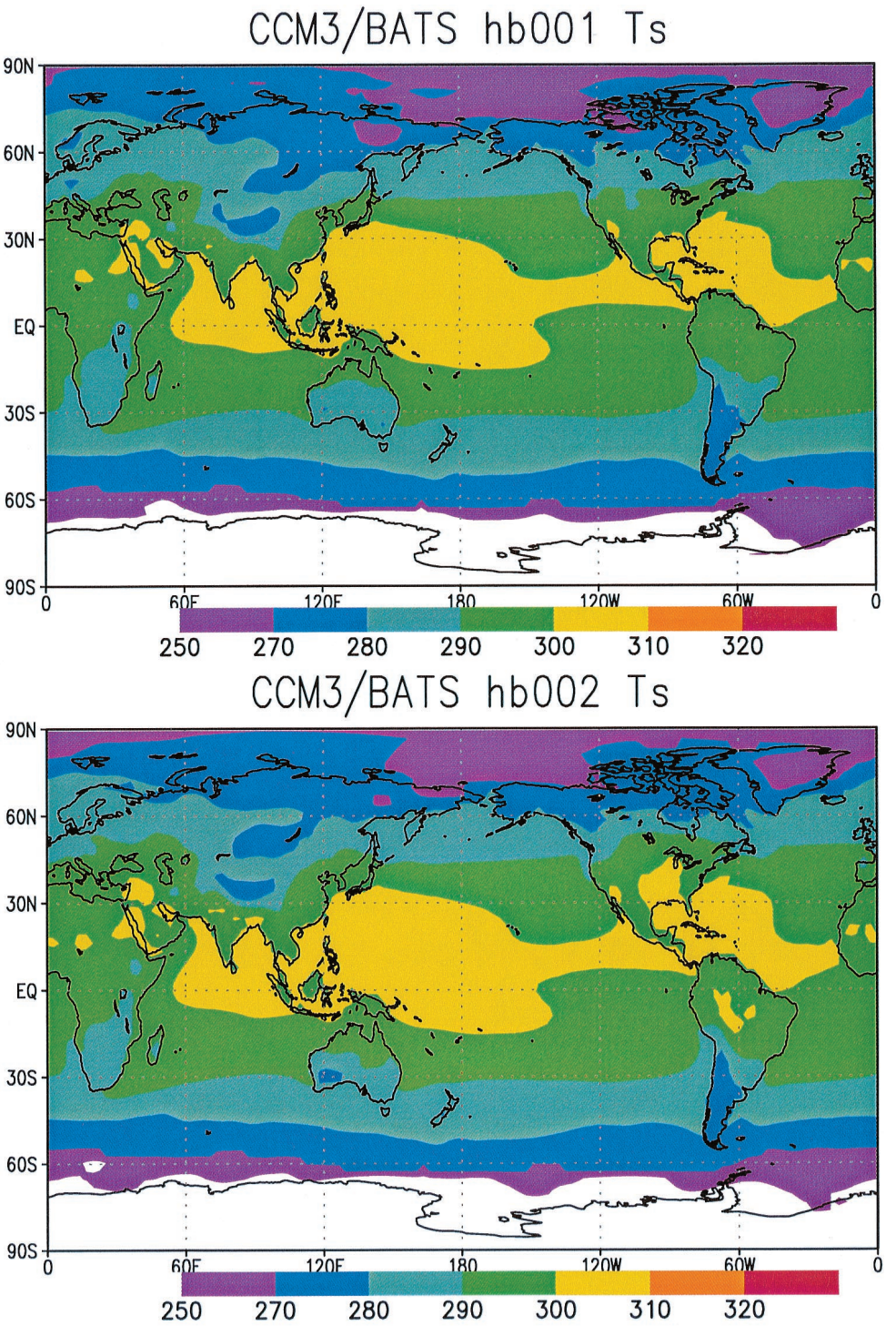

Plate 2. CCM3/BATS simulations of daily skin temperature for two continuous days in August: "hb0001" and "hb0002" represent the two days.

perature minus the algorithm-produced skin temperature presented in Plate 3. In general, with the use of accurate air temperature information, algorithm-produced skin temperature agrees very well with the "true" skin temperature. The smallest differences are observed at tropical and low latitudes where most areas are covered by ocean; the largest differences are observed around 50°N and 40°–70°S where the maximum is 2 K. Cloud systems over these areas are suggested as the determined factor for these disagreements. Large differences are noticed in high latitudes, in particular, in the winter hemisphere. This may be due to the few number of land points in the pole area or weakness of our algorithm under these conditions.

How air temperature affects the accuracy of the algorithm is indicated in Plate 4b which compares the zonal mean of skin temperature difference with and without the use of an accurate air temperature. The no-air-temperature case means that no-air-temperature simulations have been used. Rather, the algo-

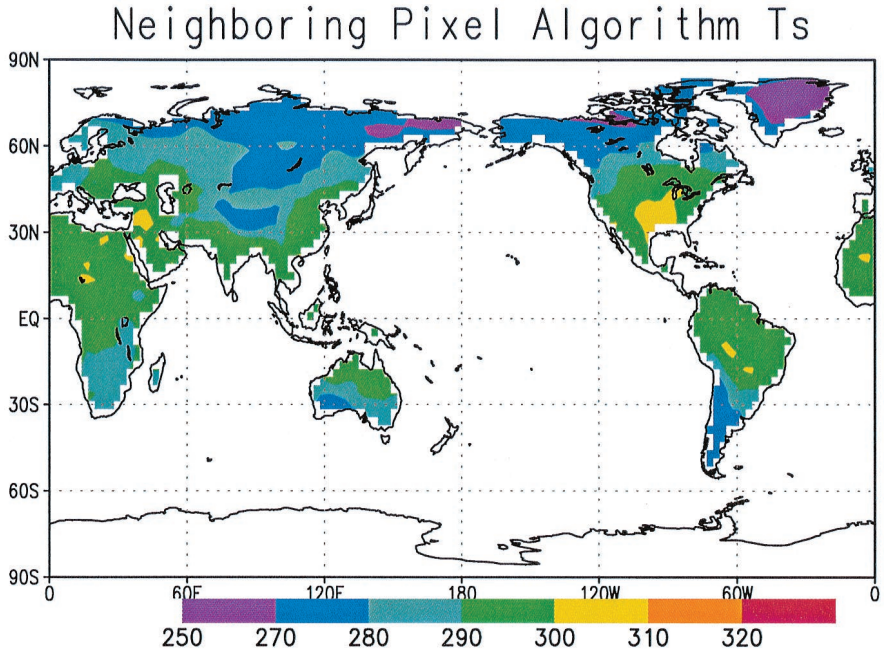

Plate 3. Evaluation of global application of the "neighboring-pixel" approach. The presented skin temperature is produced by "neighboring-pixel" algorithm for day "hb0001," based on air temperature, wind speed, and the difference of solar radiation between "hb0001" and "hb0002." See text for details.

rithm uses a simple linear relationship between air and skin temperatures:

$$T_a = bT_s, \tag{20}$$

where $b \leq 1$ during daylight hours and $b \geq 1$ at night. At most latitudes both cases are very similar with an accuracy between ± 1 and 3 K. However, high latitudes of the winter hemisphere give a relatively large error, with a maximum as much as 5–7 K. From this analysis the algorithm appears to be applicable globally when accurate air temperatures are unknown.

Since global, pixel-level air temperature data sets are not available, use of relationships between T_a and T_s is desirable but may not be derivable for all surfaces because of the complexity of this problem. The relationship between T_a and T_s strongly depends on surface roughness, topographical properties, soil moisture, and atmospheric states. Currently, no

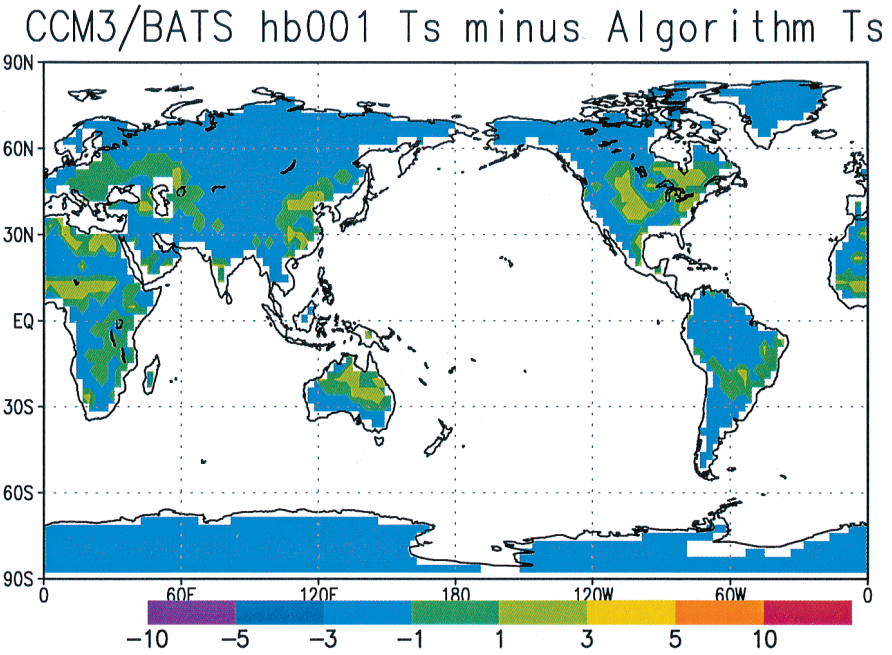

Plate 4. Difference field of algorithm-produced global skin temperature and its CCM3/BATS simulations for day "hb0001."

method or boundary layer theory can adequately describe this relationship. Some well-accepted relationships may be useful as constraints in our algorithm. For example, T_a is lower than T_s for daytime and usually higher than T_s at nights for clear sky; also, T_a is close to T_s for cloudy nights [*Jin et al.*, 1997].

Effects of cloud cover on sea surface skin temperature (SST) may also be estimated (not shown), although the algorithm is originally developed for land surface. Moreover, this algorithm can be applied over high latitudes in the winter hemisphere when there is no surface insolation, whereas the Jin99 requires information on surface insolation thus could not be used for polar regions or at night.

4.3. Error Analysis

Error analysis indicates the errors induced into the final result by the uncertainty in different variables, for our case, including surface net solar radiation, air temperature, wind speed, and α for Bowen ratio which are used to derive T_s^{cld}. The sensitivities of the algorithm to the above mentioned variables are examined by using FIFE data.

Figure 7a is the rms error in T_s^{cld} versus the variations of net surface solar radiation through fraction f,

$$S_n' = f \times S_n, \tag{21}$$

where S_n is the accurate surface net solar radiation, and S_n' is the actual surface radiation used. The rms error only increases moderately, from 0.87 to 1.3 K, for solar radiation variation as much as 30%. Apparently, the uncertainty in solar radiation causes little significant error in the final results of T_s^{cld}. One possible reason is that although surface temperature is very sensitive to the solar insolation, the difference between clear and cloudy skin temperature is also influenced by longwave radiation, sensible, and latent heat fluxes. Some of the variations of these terms might compensate each other and reduce the variability of T_s^{cld} and have less variations. More importantly, in this error analysis, T_a^{cld}, T_a^{clr}, and T_s^{cld} are fixed, with only ΔS_n varying. Constraining these temperatures may already incorporate most of the dependence of T_s^{clr} on solar radiation. In addition, the increase of error may be significant (by 150% in rms ratio), but as long as the value of temperature is of interest, an accuracy of 1.3 K in T_s^{cld} is acceptable.

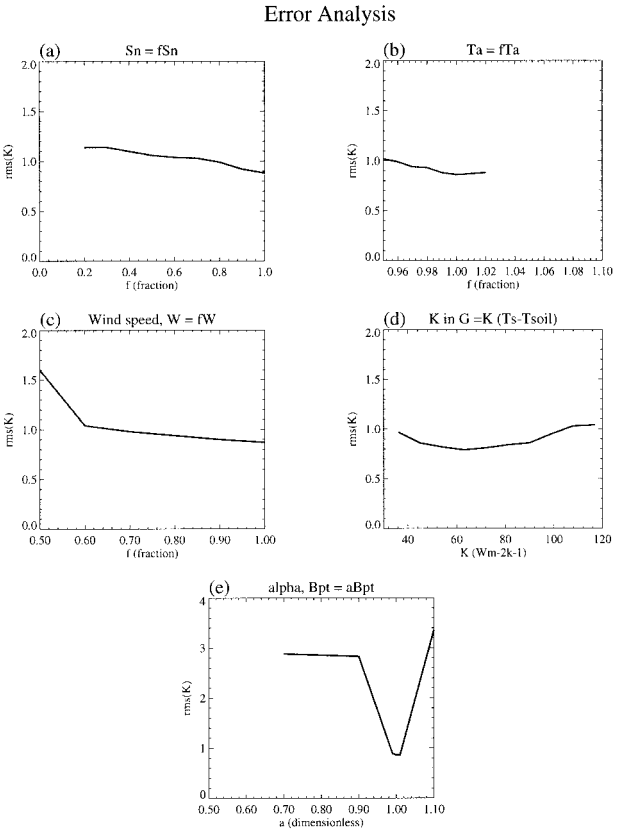

Figure 7. Error analysis of the algorithm. RMS error versus variation of (a) solar radiation (W m^{-2}), (b) air temperature (°C), (c) wind speed (ms^{-1}), (d) ground heat flux coefficient K (W m^{-1} K^{-1}), and (e) α for Priestly-Taylor Bowen ratio.

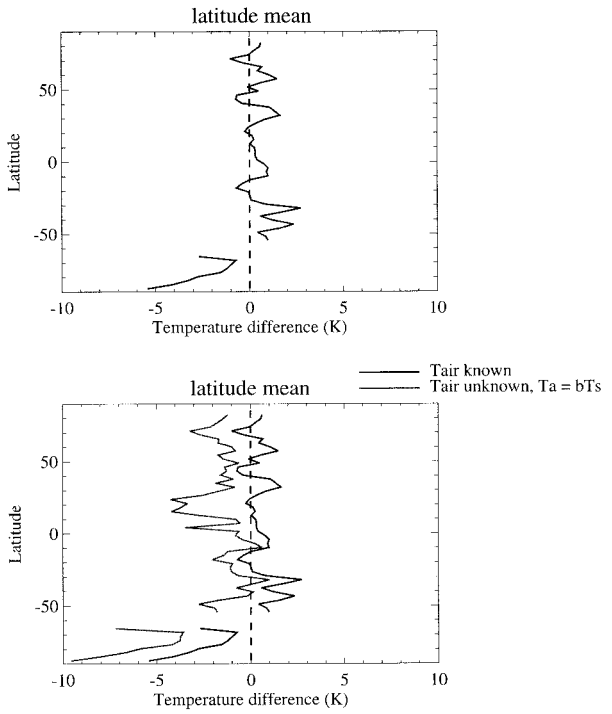

Figure 6. (a) Zonal mean of the difference field presented in Plate 3. (b) Comparison of algorithm-produced skin temperature with and without use of air temperature.

Similarly, using

$$T_a' = f \times T_a, \tag{22}$$

we can study the sensitivity of the algorithm to air temperature T_a, as shown in Figure 7b. The pattern of T_a seems to have a larger effect than its magnitude on the final accuracy of the skin temperature. For T_a varying by 2%, corresponding to a 10–15 K increase, the rms varies but little, from 0.9 to 1.0 K. In contrast to Figure 3, which uses an inaccurate air temperature in both pattern and magnitude, Figure 7b uses the correct air temperature pattern but with a change in magnitude. The small rms implies that the algorithm may not be very sensitive to air temperature if the pattern of air temperature is correct. Similarly, error analysis of wind speed (Figure 7c) and the coefficient of ground heat flux, K, are shown in Figures 7c and 7d. The accuracy of the algorithm is not significantly affected by either of them.

Large sensitivity, however, is observed for α in $B_{PT}(\alpha, T)$ (Figure 7e). The change (more than 5% in α) results in error increases from 1 to 3 K. The sensitivity of the algorithm to α

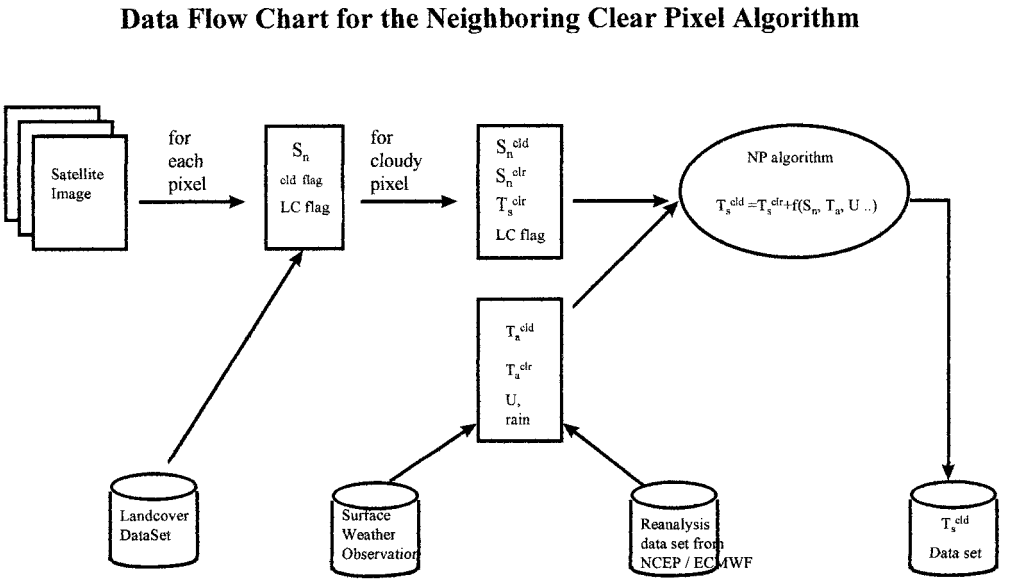

Figure 8. Data flowchart of how to use "neighboring-pixel" algorithm for satellite data.

suggests the necessity for a good estimate of α. At this point, α and Bowen ratio $B_{PT}(\alpha, T)$ are major sources of error. Improved methods to estimate the Bowen ratio are expected to improve this aspect.

5. Discussion and Conclusions

Clouds span temporal scales on the order of hours to several days and spatial scales of 10 to thousands of kilometers. Hence deriving a generally acceptable relationship between clouds and skin temperature may be problematical. Surface energy balance (SEB) is a good starting point to study the influences of clouds on surface skin temperature. As this work shows, writing each energy term in terms of skin temperature, we can infer cloudy surface skin temperature from its neighboring clear pixel skin temperature plus other information such as surface insolation, air temperature, and wind speed.

The present proposed algorithm differs from the preceding Jin99 by parameterizing sensible, latent fluxes, and net longwave radiation in terms of skin temperature rather than net solar radiation. With the use of surface energy balance and the "neighboring pixel" algorithm, skin temperature of a cloudy pixel can be determined, even under circumstances such as nights and high latitudes where no solar insolation is available. Similar to Jin99, this treatment still uses "air temperature" but includes it in the "neighboring-pixel" algorithm, instead of using the "air temperature adjustment" technique. This modification reduces the dependence on an accurate air temperature data, which may be very difficult to obtain for an inhomogeneous land surface. This generalized method may provide estimates at each pixel with an accuracy as good as 1–2 K for a monthly mean but degraded to above 2 K during precipitation.

Because satellite thermal infrared sensors cannot measure cloud-covered surface skin temperature, the goal of our work is to develop an algorithm that could derive cloudy pixel skin temperature (T_s^{cld}) from other available variables, including clear pixel skin temperature (T_s^{clr}), air temperature (T_a^{clr}, T_a^{cld}), wind speed (U), surface insolation (ΔS_n), and heat fluxes between clear and cloudy pixels. Figure 8 is a data flowchart that demonstrates how to apply our proposed algorithm to satellite data in some routine fashion. After receiving a satellite image we calculate surface insolation for each pixel using *Pinker and Ewing* [1985] or *Li et al.* [1993] technique. A land cover flag will be obtained for each pixel from a land cover data set. Then for each cloudy pixel, we search neighboring clear pixel(s) over a similar land cover and latitudes. From global weather station routine observations or from numerical weather prediction forecasts (i.e., National Centers for Environmental Prediction (NCEP), European Centre for Medium-Range Weather Forecasts (ECMWF)) we need to obtain surface air temperature and wind speed information. Then, input all the above known information into our algorithm to calculate T_s^{cld}.

Although this proposed "neighboring-pixel" method may be most practical in calculating skin temperature for a cloudy pixel, and thus to improve the satellite skin temperature data sets, it still suffers from several deficiencies. (1) Data scaling: No global pixel-level air temperature and wind speed data sets are available to match satellite skin temperature temporal and spatial scales. The best available data sets for these variables, probably, are reanalysis or interpolated surface observations. (2) Algorithm assumption: Several climatological assumptions may be valid for typical surface or boundary situations but not for extreme cases. For example, the Bowen ratio depends on various factors from soil moisture to vegetation density. When precipitation occurs, changes of soil wetness and air humidity result in a different Bowen ratio. The method applied in this algorithm has difficulty in capturing such changes explicitly.

Research conducted concerning the use of this algorithm on the satellite data sets will lead to generation of better satellite data sets, not only for EOS MODIS in the future but also for other satellites that use thermal infrared channels to observe surface skin temperature, such as GOES and Landsat.

Acknowledgments. We thank the two anonymous reviewers for their professional and insightful comments. This work is supported by

the NASA EOS Interdisciplinary Scientific Research Program (U.P.N. 429-82-22; U.P.N. 428-81-22).

References

Blanken, P. D., T. A. Black, and P. C. Yang, Energy balance and canopy conductance of a boreal aspen forest: Partitioning, overstory, and understory components, *J. Geophys. Res*., *102*, 28,915–28,927, 1997.

Betts, A. K., and J. H. Ball, The FIFE surface diurnal cycle climate, *J. Geophys. Res*., *100*, 25,679–25,693, 1995.

Brunt, D., Notes on radiation in the atmosphere, *Q. J. R. Meteorol. Soc*., *58*, 389–418, 1932.

Brutsaert, W., On a derived formula for long-wave radiation from clear skies, *Water Resour. Res*., *11*, 742–744, 1975.

Brutsaert, W., *Evaporation Into the Atmosphere*, 299 pp., D. Reidal, Norwell, Mass., 1982.

Culf, A. D., and J. C. Gash, Longwave radiation from clear skies in Niger: A comparison of observations with simple formulas, *J. Appl. Meteorol*., *32*, 539–547, 1993.

Deardorff, J. W., Efficient prediction of ground surface temperature and moisture, with inclusion of a layer of vegetation, *J. Geophys. Res*., *83*, 1889–1903, 1978.

Dickinson, R. E., The force-restore model for surface temperatures and its generalization, *J. Clim*., *1*, 1086–1097, 1988.

Dickinson, R. E., *Land Surface Processes*, *Climate System Modeling*, Cambridge Univ. Press, New York, 1992.

Frouin, R., C. Gautier, and J. Morcrette, Downward longwave irradiance at the ocean surface from satellite data: Methodology and in situ validation, *J. Geophys. Res*., *93*, 597–619, 1988.

Fu, Q., and K. N. Liou, On the correlated κ-distribution method for radiative transfer in nonhomogeneous atmospheres, *J. Atmos. Sci*., *49*, 2139–2156, 1992.

Fung, I., D. E. Hassion, and A. A. Lacies, On the variability of the net longwave radiation at the ocean surface, *Rev. Geophys*., *22*, 177–193, 1984.

Garratt, J. R., *The Atmospheric Boundary Layer*, Cambridge Univ. Press, New York, 1992.

Hatfield, J. L., R. J. Reginato, and S. B. Idso, Comparison of long-wave radiation calculation methods over the United States, *Water Resour. Res*., *19*, 285–288, 1983.

Idso, S. B., and R. D. Jackson, Thermal radiation from the atmosphere, *J. Geophys. Res*., *74*, 5397–5403, 1969.

Jin, M., Interpolation of surface radiation temperature measured from polar orbiting satellites to a diurnal cycle, 2, Cloudy-pixel treatment, *J. Geophys. Res*., *105*, 4061–4076, 2000.

Jin, M., and R. E. Dickinson, Interpolation of surface radiative temperature measured from polar orbiting satellites to a diurnal cycle, 1, Without clouds, *J. Geophys. Res*., *104*, 2105–2116, 1999.

Jin, M., R. E. Dickinson, and A. M. Vogelmann, A comparison of CCM2/BATS skin temperature and surface-air temperature with satellite and surface observations, *J. Clim*., *10*, 1505–1524, 1997.

Li, Z., H. G. Leighton, K. Masuda, and T. Takashima, Estimation of SW flux absorbed at the surface from TOA reflected flux, *J. Clim*., *6*, 317–330, 1993.

Masuda, K., H. G. Leighton, and Z. Li, A new parameterization for the determination of solar flux absorbed at the surface from satellite measurements, *J. Clim*., *8*, 1615–1629, 1995.

Pinker, R. F., and J. A. Ewing, Modeling surface solar radiation: Model formulation and validation, *J. Climatol. Appl. Meteorol*., *24*, 389–401, 1985.

Priestley, C. H. B., and R. J. Taylor, On the assessment of surface heat flux and evaporation using large-scale parameters, *Mon. Weather Rev*., *100*, 81–92, 1972.

Sellers, P. J., F. G. Hall, G. Asrar, D. E. Strebel, and R. E. Murphy, An overview of the First International Satellite Land Surface Climatology Project (ISLSCP) Field Experiment (FIFE), *J. Geophys. Res*., *97*, 18,345–18,371, 1992.

Sellers, P. J., et al., The Boreal Ecosystem-Atmosphere Study (BOREAS): An overview and early results from the 1994 field year, *Bull. Am. Meteorol. Soc*., *76*, 1549–1577, 1995.

Shuttleworth, W. J., Evaporation, chap. 4, in *Handbook of Hydrology*, edited by David R. Maidment, McGraw-Hill, New York, 1992.

Stull, R. B., *An Introduction to Boundary Layer Meteorology*, 670 pp., Kluwer Acad., Norwell, Mass., 1988.

Susskind, J., Water vapor and temperature, in *Atlas of Satellite Observations Related to Global Change*, pp. 89–128, Cambridge Univ. Press, New York, 1992.

Swinbank, W. C., Long-wave radiation from clear skies, *Q. J. R. Meteorol. Soc*., *89*, 339–348, 1963.

Thom, A. S., Momentum, mass and heat exchange of plant communities, *Q. J. R. Meteorol. Soc*., *193*, 345–357, 1972.

R. E. Dickinson, Earth and Atmospheric Sciences, Georgia Institute of Technology, 221 Bobby Dodd Way, Atlanta, GA 30332-0340.

M. Jin, Department of Meteorology, University of Maryland, College Park, MD 20742. (mjin@metosrv2.umd.edu)

(Received August 26, 1999; revised March 14, 2000;
accepted April 26, 2000.)